Nanoscale

COMMUNICATION

View Article Online
View Journal | View Issue

Cite this: *Nanoscale*, 2026, **18**, 6264

Received 16th August 2025,
Accepted 7th February 2026

DOI: 10.1039/d5nr03481g

rsc.li/nanoscale

Surface plasmon resonance as a breakthrough tool for characterizing the size and shape of graphene quantum dots

Giuseppe Stefano Basile,[a] Damiano Calcagno,[a] Nunzio Tuccitto,[a] Benoit Maxit,[b] Pascal Boulet,[c] Mélanie Emo,[c] Liang Liu,[d] Giuseppe Grasso *[a] and Philippe Pierrat *[e]

Graphene quantum dots (GQDs) exhibit size- and shape-dependent properties that critically influence their optical and electronic behavior, yet their reliable nanoscale characterization remains challenging. Here, we introduce a diffusion-based surface plasmon resonance (*D*-SPR) workflow that enables quantitative, shape-sensitive characterization of GQDs beyond conventional spherical approximations. Using sustainably synthesized GQDs derived from banana peels *via* optimized microwave-assisted methods, *D*-SPR resolves distinct particle populations, distinguishing monodisperse disk-like GQDs with average lateral dimensions of ≈2.5 nm from larger, polydisperse structures averaging ≈20 nm. These results are in excellent agreement with HR-TEM and DLS measurements. Crucially, unlike conventional DLS, *D*-SPR exploits diffusion–geometry coupling to directly identify non-spherical, disk-like GQD morphologies, supported by computational and mathematical modeling. This label-free approach delivers rapid, high-sensitivity size and shape resolution using minimal sample volumes, establishing *D*-SPR as a powerful complementary tool for the advanced characterization of carbon-based nanomaterials.

1. Introduction

Graphene quantum dots (GQDs) are zero-dimensional carbon nanomaterials with tunable size-dependent properties,[1] high solubility, and low toxicity,[2] making them attractive for sensing, catalysis, and bioimaging applications. Accurate determination of GQD size and morphology remains challenging due to their small lateral dimensions and limited contrast in conventional imaging techniques.

Graphene quantum dots can be prepared *via* a wide variety of synthetic strategies, broadly classified into top-down and bottom-up approaches.[3] In that context, we recently reported a straightforward synthetic process allowing for the preparation of GQDs from various biomass wastes under microwave heating.[4] Herein, GQDs were prepared from banana peels using a simple two-step acid treatment, yielding high-purity nanoparticles suitable for size characterization.

Despite the development of modern instruments, characterization of 0D materials such as graphene quantum dots remains particularly challenging and requires specialized techniques that can provide accurate size measurements and morphology determination at the nanoscale. Accurate size characterization of GQDs remains challenging. Conventional techniques such as dynamic light scattering (DLS), atomic force microscopy (AFM), scanning electron microscopy (SEM), and high-resolution transmission electron microscopy (HR-TEM) provide valuable information, but each has limitations. DLS measures hydrodynamic diameter, which can differ from the actual size due to aggregation and is best suited for spherical, monodisperse particles. AFM and HR-TEM provide direct size measurements, but require careful sample preparation, are limited in throughput, and can have low contrast for thin carbon-based nanoparticles. SEM lacks sufficient resolution for nanoscale GQDs. Consequently, complementary methods are needed to obtain accurate, high-throughput size measurements.

Herein, we describe the synthesis of two batches of biomass-derived GQDs with distinct size characteristics, and their size characterization is carried out, for the first time, by diffusion-surface plasmon resonance (*D*-SPR).[5–9] This method allows the calculation of diffusion coefficient (*D*) values of solutes in a flow-based system and relies on the principle of Taylor dispersion analysis (TDA),[10] but it has broader application and increased sensitivity due to the SPR detector, which relies on changes in the refractive index of the molecule under analysis. Indeed, traditionally, TDA relies on either ultraviolet

[a]*Department of Chemical Sciences, University of Catania, Viale Andrea Doria 6, Catania, Italy. E-mail: grassog@unict.it*
[b]*Cordouan Technologies, Cité de la Photonique, 11 Avenue Canteranne, F-33600 Pessac, France*
[c]*Institut Jean Lamour, Université de Lorraine, CNRS, UMR 7198, F-5400 Nancy, France*
[d]*University of Lorraine, CNRS, Laboratoire de Chimie Physique et Microbiologie pour les Matériaux et l'Environnement (LCPME), Nancy F-54000, France*
[e]*Université de Lorraine, CNRS, Laboratoire Lorrain de Chimie Moléculaire (L2CM), UMR 7053, F-54000 Nancy, France*

(UV) absorbance or fluorescence-based detection. These conventional approaches, however, introduce significant limitations when applied to nanomaterials with inherently low extinction coefficients, such as GQDs. For UV-based detection, the sensitivity usually isn't enough to accurately measure low levels of small carbonaceous species. Fluorescence detection, however, provides higher sensitivity but requires either naturally fluorescent samples or the addition of external fluorescent tags. This requirement not only complicates sample preparation, but also introduces potential alterations to the nanoparticles physicochemical properties, thereby limiting the authenticity of the measurement.

D-SPR, on the other hand, has been designed to be a label-free, real time method to determine diffusion coefficients through the measurement of concentration profiles evolution over time.

Zingale and colleagues designed and benchmarked the efficacy of *D*-SPR on small to medium sized systems, showing that high precision is achievable using commercially available benchtop instruments,[6,11] even for molecules mixtures.[12]

In this paper, the results from the *D*-SPR analysis were consistent with HR-TEM and DLS findings, providing complementary information on particle size distribution that remains challenging to obtain with conventional techniques.

2. Experimental

2.1. Graphene quantum dots synthesis

2.1.1. Preparation of GQDs-01. Dried powder of banana peels (200 mg) was suspended in concentrated H_2SO_4 (16 mL) in a G30 reaction tube and subjected to carbonization under microwave-assisted heating in a Monowave 450 device (Anton Paar) at 180 °C for 5 min. After being cooled, the reaction medium was carefully diluted in water (200 mL), and the dark carbonized suspension was recovered by centrifugation and subsequently dried at 70 °C for 48 h. In the second step, the carbonized powder (50 mg) was heated with conc. HNO_3 (5 mL) in a G30 reaction vessel at 150 °C for 5 min. After cooling and concentration to dryness, GQDs-01 were obtained as a brownish solid (17 mg, 34%).

2.1.2. Preparation of GQDs-02. The carbonized powder derived from banana peels described for GQDs-01 (100 mg) was suspended in concentrated HNO_3 (10 mL) and stirred at room temperature for 4 days. After concentration to dryness, GQDs-02 (85 mg, 85%) were recovered as a dark powder.

2.2. Surface plasmon resonance

A theoretical description of *D*-SPR is available in Basile *et al.* and is here summarized for the sake of clarity.[9]

In brief, *D*-SPR exploits the fact that, in a pressure-driven microfluidic channel, the evolution of a dilute analyte plug concentration profile is governed by the advection-diffusion equation

$$\frac{\partial C(x,t)}{\partial t} = D\nabla^2 C(x,t) - \nabla \cdot (C(x,t)\,u(x)) \tag{1}$$

where $C(x,t)$ is the solute concentration, D the molecular diffusion coefficient and $u(x)$ the Poiseuille velocity field in a cylindrical channel of radius R. Under Taylor-Aris conditions,[10,13] a short concentration pulse injected at t = 0 gives rise, at a downstream detector, to an approximately Gaussian average concentration profile $\bar{C}(t)$ and to a corresponding detector signal $S(t)$ of the form

$$S(t) \propto \bar{C}(t) \simeq \frac{M}{(2\pi)^{3/2}R^2}\frac{1}{\sqrt{kt}}\exp\left[-\frac{(-t_r)^2}{2\sigma^2}\right] \tag{2}$$

where M is the total injected mass, t_r the mean residence time, σ^2 the temporal variance of the peak, and k a geometric factor that depends on the channel and flow conditions. In this ideal regime, the diffusion coefficient is related to the pulse broadening *via*

$$D = \frac{{t_r}^2}{24R^2\sigma^2} \tag{3}$$

In conventional SPR instruments, the microfluidic layout does not generate Dirac-like pulses but rather reproducible square plugs of analyte injected at constant flow through a loop system.[6,9,11]

For a non-interacting analyte and an optically homogeneous sensor surface, the refractive-index-based SPR sensorgram $S(t)$ is proportional to the analyte concentration profile averaged over the sampling volume of the evanescent plasmonic field. In *D*-SPR, instead of fitting $S(t)$ directly, one considers its first time derivative, which can be accurately described by an exponentially modified Gaussian (EMG)

$$\frac{\mathrm{d}S(t)}{\mathrm{d}t} = \frac{1}{\tau}\exp\left[-\frac{t-\mu}{\tau}\right] + \frac{\sigma}{\tau}\Phi\left(\frac{t-\mu}{\sigma} - \frac{\sigma}{\tau}\right) \tag{4}$$

where Φ is the standard error function, and μ, σ, and τ are fitting parameters. The EMG functional form allows one to compute the first three temporal moments of the derivative peak – the mean (m), the variance (s^2), and the skewness (sk)- as functions of μ, σ, and τ.

Within the same hydrodynamic assumptions as Taylor–Aris dispersion, these moments can be mapped back onto an effective longitudinal diffusion coefficient according to

$$D_{SPR} = \frac{R^2 m}{24s^2(1+\mathrm{sk})}. \tag{5}$$

Eqn (5) is the working formula used throughout this study to extract diffusion coefficients from *D*-SPR experiments. By construction, *D*-SPR reduces to the classical Taylor—Aris expression, when the injection profile approaches an ideal pulse and the EMG peak becomes symmetric (sk → 0), while remaining applicable to the more realistic square-plug injections of commercial SPR instruments. In practice, *D*-SPR thus provides label-free, low-volume diffusion measurements that are directly comparable across small molecules, biological macromolecules and nanoparticles, even with sizes well below the DLS limit of ≈2 nm. While both DLS and *D*-SPR ultimately derive particle sizes from diffusion coefficients, *D*-SPR offers

several practical and methodological advantages over DLS. Its pressure-driven microfluidic flow format is more robust against small temperature gradients, and it consumes a much smaller sample volume, a crucial benefit when analytes are scarce or costly. Furthermore, *D*-SPR provides higher resolution in polydisperse or multimodal samples, effectively distinguishing overlapping nanoparticle populations that conventional DLS would tend to blur together.[9,14] Because the SPR signal arises from refractive index changes rather than scattered light intensity, *D*-SPR remains sensitive to very small species, enabling accurate measurement of particles well below 2 nm, beyond the ≈1 nm lower size limit of typical DLS instruments.

Finally, fluorescent species like GQDs could produce a high background noise signal because of re-emitted fluorescent light that is generally incoherent and does not provide useful information to the DLS autocorrelation function.[15]

2.2.1 *D*-SPR instrument schematics. SPR systems used for biophysical and biochemical analyses typically share a common architecture. They include an injection unit, often a peristaltic pump coupled to a sample loop and n-way valves, designed to deliver accurate, fixed sample volumes while maintaining a continuous buffer flow. A microfluidic circuit, frequently with multiple parallel channels, then connects the injection block to the flow cell. The flow cell houses the sensor, which must meet the physical and geometrical requirements needed to generate a reliable SPR signal.[16,17]

In this work, we used an SPR Navi 210A fluidic system. The setup features two separate parallel channels, typically operated as a reference and a sample channel. The instrument is equipped with two lasers (670 nm and 785 nm). We used both wavelengths, since no appreciable differences were observed in the evolution of the SPR signal during the experiments. A scheme of a typical SPR apparatus for *D*-SPR measurements is shown in Fig. 1. From an experimental standpoint, the protocol is straightforward. Once the working concentration, the injection-volume profile, and an appropriate sensor are selected—based on sample availability, the chemical nature of the species involved, and their interaction with the sensor surface—a series of repeated injections is performed at a flow rate of about 5–10 μL min^{-1}, while recording the associated sensorgrams.[11] The signal has been numerically differentiated and fitted as reported both in the literature and in the following sections.[5,6,9,11]

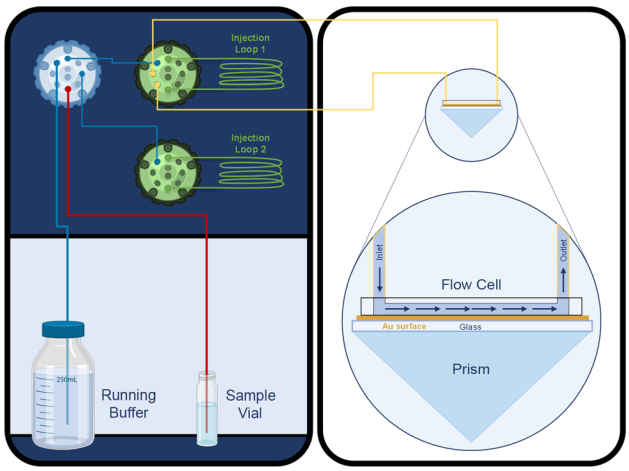

Fig. 1 Pictorial representation of an SPR apparatus for both interaction and *D*-SPR analyses, reproduced from Zingale *et al.* S1.[6,18] In the right inset a simple SPR flow cell is depicted, along with its associated gold sensor. The laser rays are omitted.

2.2.2. SPR sensor preparation. The gold surface of the SPR sensor was previously grafted with an aqueous solution of 20k mPEG-SH (2.2 mg, Laysan Bio, Inc.) in 0.9 M Na_2SO_4 under agitation for 1.5 h to avoid any nonspecific adsorption of the analyte during the *D*-SPR experiment.

2.2.3. Preparation of GQDs solutions. GQDs solutions (0.4 mg mL^{-1}) were prepared by dissolving GQDs powders in 1 mL of TRIS buffer (50 mM, pH 10.7) and filtering through a filter of 0.22 μM pore size.

2.3. Characterization of GQDs

2.3.1. High resolution transmission electron microscopy. High resolution transmission electron microscopy (HR-TEM) investigations were carried out using a JEOL JEM—ARM 200F Cold FEG TEM/STEM operating at 200 kV and equipped with a spherical aberration (C_s) probe and image correctors (point resolution 0.12 nm in TEM mode). Grids were prepared by placing a drop of GQD solution (200 μg mL^{-1} in pure water) on a carbon-coated copper grid (200 mesh size) for four minutes. The drop was then removed by mean of a filter paper and the grid let to dry at room temperature for five minutes, then at 80 °C overnight. A batch of images (a total of 140 particles were randomly selected) permitted to elaborate a particle size distribution.

2.3.2. Atomic force microscopy (AFM). The AFM measurements were performed on Nanosurf DriveAFM using SCANASYST-AIR-HR probe in dynamic mode. The dispersions of GQDs with 1 mg mL^{-1} concentration were dropcast on silicon wafer. Imaging was carried out at 30% deflection of the tip.

2.3.3. Dynamic light scattering. The average particle size of GQDs was measured by DLS using a VASCO KIN Particle Size Analyzer apparatus (Cordouan Technologies, Pessac, France). All measurements were performed on freshly prepared suspensions diluted in ethanol, at 25 °C, and in triplicate. Data were analysed using the multimodal number distribution of the Nano Kin®software supplied with the instrument and expressed as mean (±SD).

2.3.4. *D*-SPR analysis. The average diffusion coefficient of GQDs-01 and GQDs-02 has been determined by the *D*-SPR technique described by Zingale *et al.*[6,11] The instrument configuration features two distinct and parallel fluidic channels, one typically designated as the reference channel and the other as the sample channel. Two lasers, emitting at wavelengths of 670 nm and 785 nm, respectively, are integrated into the system. Both wavelengths were employed in the experiments, as no significant differences in the SPR signal evol-

ution were observed between them. The experiments utilized a previously described PEG-functionalized sensor. Each sensor chip measures 20 mm in length, 12 mm in width, and 0.55 mm in thickness, with a contact area of 12 mm^2. SPR measurements were carried out using the SPR Navi 210A fluidic system. This system comprises a 1 μL flow cell with tubing connectors and a dual-channel syringe pump that manages two independent flow paths, one for each measurement chamber. Buffer solution flows from its container through an injection valve system into the respective measurement chambers of the flow cell and is then directed to a waste bottle. A separate syringe pump automates the loading and cleaning of the sample loops. The PEEK tubings connecting the sample loop to the flow cell are 70 cm long and have an internal diameter of 254 μm. GQDs-01 solution was prepared by dissolving 0.88 mg of powder in 1 mL of the running buffer (TRIS 50 mM, pH 10.7), then filtered with a syringe to remove the undissolved particles (0.22 μM pore size) and diluted to a final concentration of 0.44 mg mL^{-1}. GQDs-02 solution was prepared by dissolving 0.77 mg of powder in 1 mL of the running buffer (TRIS 50 mM, pH 10.7), then filtered with a syringe to remove the undissolved particles (0.22 μM pore size) and diluted to a final concentration of 0.4 mg mL^{-1}. The high hydrophobic content of the molecules under analysis required several trials to identify a proper non-interacting surface as described in section 2.2.1.

3. Results and discussion

GQDs were synthesized from biomass waste, specifically here from banana peels, using a two-steps microwave-assisted process. The first step involved carbonizing the dried biomass in sulphuric acid at 180 °C, followed by treatment of the resulting carbonaceous intermediate with concentrated nitric acid. In our original procedure, this second step was carried out at 150 °C for 5 minutes, yielding a batch referred to as GQDs-01. By contrast, performing the same step at room temperature over four days produced a second batch, GQDs-02, with an almost quantitative yield. XPS analysis (Fig. S1 and S2) demonstrated that GQDs-01 and GQDs-02 have nearly identical chemical compositions, characterized by comparable elemental fractions of C (65%), O (30%), and N (5%). Consistently, the FT-IR spectra of both samples (Fig. S6) display closely overlapping profiles, characterized by broad bands in the 3300–3500 cm^{-1} region attributable to O–H stretching vibrations of carboxylic groups, a pronounced C=O stretching mode at approximately 1680 cm^{-1}, and a band at around 1480 cm^{-1} assigned to C–O stretching. Furthermore, photophysical characterization reveals conventional steady-state absorption (Fig. S7) and photoluminescence (Fig. S8) features for both carbon-based materials, in good agreement with those typically reported for graphene quantum dots.[19] Despite these closely similar chemical and photophysical characteristics, GQDs-01 and GQDs-02 exhibit marked differences in particle size and morphology. These differences were consistently confirmed by high-resolution transmission electron microscopy (HR-TEM), Fast Fourier Transform (FFT) analysis, and dynamic light scattering (DLS) measurements (Fig. 2). GQDs-01 appeared as well-dispersed nanoparticles with an average diameter of 2.5 ± 0.7 nm as determined by TEM, in excellent agreement with the 2.5 ± 0.4 nm measured by DLS, although the near-identical numerical values are coincidental. In contrast, GQDs-02 consist of significantly larger, yet still well-dispersed, particles measuring 21.0 ± 5.2 nm by HR-TEM and 32.1 ± 5.4 nm by DLS. Structural differences between the two samples are further highlighted by FFT analysis. The FFT pattern acquired from an individual GQDs-01 particle (Fig. 2b) displays well-defined diffraction spots, consistent with a single-crystalline domain and *d*-spacings matching those of a graphitic lattice ($P6_3/mmc$, $a = b = 2.5$ Å, $c = 6.7$ Å). In contrast, GQDs-02 exhibit only a diffuse halo ring in the FFT pattern for all analyzed particles (Fig. 2f), indicating an amorphous structure. The absence of long-range crystallinity in GQDs-02 is likely related to their room-temperature synthesis, as the formation of well-ordered graphitic domains generally requires elevated temperatures. XRD analyses were performed on both samples (Fig. S4). In both cases, a broad diffraction peak centered around 21° is observed and can be assigned to the graphitic-like (002) plane of graphite, indicating the presence of short-range graphitic ordering at the solid state within the carbonaceous frameworks of both GQDs-01 and GQDs-02. These results are consistent with results reported in the literature for GQDs synthesized by other methodologies.[20,21] The broad nature of the peak arises from the small lateral

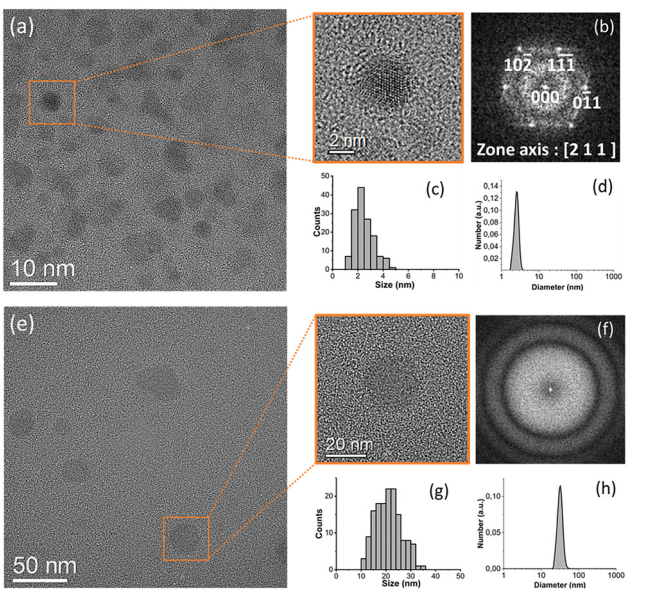

Fig. 2 HRTEM and DLS characterization of the synthesized graphene quantum dots (GQDs). Panels (a–d) show high-resolution imaging, FFT pattern, size distribution built on a batch of 140 particles, and corresponding DLS-derived diameter distribution for the small-sized GQDs-01. Panels (e–h) display the analogous analyses for the larger GQD population GQDs-02.

Table 1 Results obtained through *D*-SPR analysis at 22 °C: D_{SPR} value stands for the experimental *D* obtained with its associated standard deviation of 4 experimental replicates; $r_{H_{D\text{-}SPR}}$ and $d_{H_{DLS}}$ refer to the classical Stokes–Einstein estimates of the hydrodynamic radiuses and diameters from *D*-SPR and DLS measurements, respectively. *a* and *b* refer to the minor and major axes calculated from *D* values (D_{SPR} for GQDs-01 and D_2 for GQDs-02) through modified Stokes–Einstein equations. Standard Deviations over b_{TEM} (mean diameter determined on batches of 140 individual particles) were chosen to approximate the observed size dispersity of the samples

Sample	$D_{SPR} \times 10^{-10}$ ($m^2\ s^{-1}$)	$D_{deconv} \times 10^{-10}$ ($m^2\ s^{-1}$)	a_i (nm)	$r_{H_{D\text{-}SPR}}$ (nm)	$d_{H_{DLS}}$ (nm)	b_{TEM} (nm)
GQDs-01	5.63 ± 0.15	—	a_1 = 0.11 ± 0.09 a_2 = 0.85 ± 0.34 a_3 = 0.20 ± 0.16	2.61 ± 0.01	2.5 ± 0.4	2.61 ± 0.7
GQDs-02	2.70 ± 0.12	D_1 = 5.63 ± 0.15 D_2 = 1.25 ± 0.07	a_1 = 0.14 ± 0.06 a_2 = 0.90 ± 0.40 a_3 = 0.25 ± 0.15	— 11.8 ± 0.7	32.1 ± 5.4	21.0 ± 5.2

dimensions of the GQDs, while the larger interlayer spacing compared to graphite is most likely attributable to the high density of oxygen-containing functional groups within their structures.

Finally, AFM measurements (Fig. S5) confirm that the thickness of GQDs-01 is smaller than that of GQDs-02. These results are in line with TEM and DLS results, revealing a narrow height distribution of only a few nanometers for GQDs-01, whereas substantially larger particles with average dimensions of approximately 20 nm are observed for GQDs-02.

D-SPR results further confirm previous assumptions about the average dimensions of GQDs, while also providing additional insights into the samples composition, overcoming some of the limitations of the above described techniques. From the results of 4 injections in two microfluidic channels with two different lasers, we obtained a first estimate of the *D* values for GQDs-01 and GQDs-02, as summarized in Table 1. Data analysis on the sensorgrams (Fig. S3) has been carried out according to references,[6,11] with a small variation regarding sample GQDs-02. In this case, given the larger polydispersity of the sample, we were able to individuate at least two major components of the GQDs population, one containing smaller particles, of dimensions comparable to that of GQDs-01, and a second fraction associated with the larger particles, of size ≈20 nm.

Under this assumption, the GQDs-02 signal first derivative (Fig. 3) was modeled as a convolution of two exponentially modified Gaussian functions. Multiple peak fitting was performed using the OriginPro software package,[22] employing the Levenberg–Marquardt algorithm. During this process, parameters related to the diffusion coefficient for the smaller-sized GQDs-01 were fixed based on prior determinations. Guided by the fitting parameters obtained from the GQDs-01 experiments, we were able to resolve two distinct diffusion coefficients (D_1 and D_2), as summarized in Table 1.

Starting from the observed *D* values, we went on to estimate the shape of the quantum dots. We assumed, based on the TEM observations, that the "disk-like" nature of GQDs could be well approximated by an oblate spheroid of thickness (minor semi-axis) *a* and diameter (degenerate major semi-axes) *b*.

For both samples, the *D* values have been used to derive estimates starting from a plausible distribution of diameters. The diffusion coefficient of rigid bodies in a solvent is well described by various modifications of the classical Stokes–Einstein[23–25] equation.

$$D = \frac{k_B T}{6\pi\eta r_{eq}} \cdot f(p) \tag{6}$$

where k_B is the Boltzmann constant, T is the absolute temperature, η is the solvent viscosity, $r_{eq} = (a \cdot b^2)^{1/3}$ is the equivalent hydrodynamic radius, $p = b/a$ is the aspect ratio, and $f(p)$ is a shape-dependent friction factor which depends on the particular theory under examination.

Countless theoretical efforts have been directed to the description of general shapes of particles and molecules in terms of microfriction factors.[26] We decided to implement three different models of $f(p)$ in a simple Python code that attempts to infer the unknown axis length (either *b* given a or *vice versa*) from a measured diffusion coefficient D_{target}.

The following models were employed:

- **Hydraulic–radius (original) model**, based on a sphere of equivalent hydraulic radius r_{eq} and the Stokes–Einstein relation.[23]
- **Perrin's analytical solution** for spheroids and **Gierer's microfriction theory**, which use elliptic–integral expressions and friction coefficients to account exactly for shape anisotropy and solvent interactions.[26,27]
- **Modern (Tirado–de la Torre) correction**, an empirical polynomial in $\ln(p)$ fitted to bead–model hydrodynamic simulations, valid for moderate aspect ratios ($2 \lesssim p \leq 10$), and smoothly joined to an asymptotic slender-body form $\frac{3/2 \ln p}{\ln p - 0.5}$ for $p > 10$.[28–30]

This last model should be the best option for larger GQDs since it is grounded in extensive physical simulations for all aspect ratios and could be regarded as the golden standard for disk-like particles.[28] The Python code performs a simple optimization task, employing the Levenberg–Marquardt algorithm to find the optimal *a* value which minimizes the difference between an experimentally measured *D* coefficient and the one predicted by the chosen model. We assumed that the TEM values had approximate uncertainties equal to their distributions FWHM.

We also applied the classical Stokes–Einstein equation to *D*-SPR results to infer the equivalent hydrodynamic radius and compare it to the DLS size distribution mode. Considering the

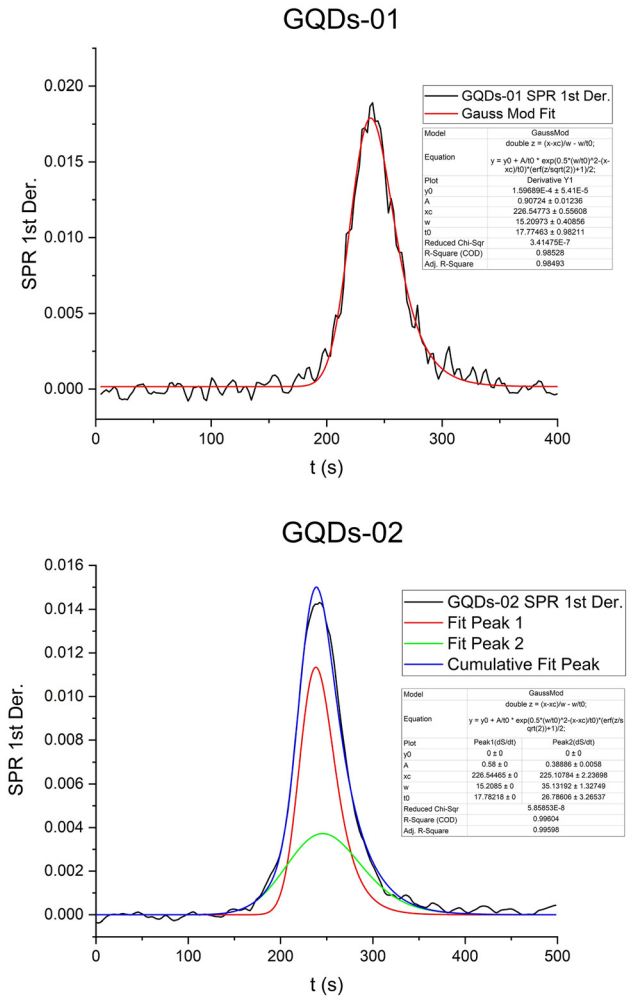

Fig. 3 First derivative SPR responses and fitted curves for GQD samples. Top: GQDs-01 shows a single, symmetric peak (black) well described by one exponentially modified Gaussian (red). Fit details are reported in the inset. Bottom: GQDs-02 shows a broad, asymmetric peak (black) fitted with two exponentially modified Gaussians—Peak 1 (red), Peak 2 (green), and their convolution (blue). Fit parameters are shown in the inset.

uncertainties, a good agreement is obtained for both GQDs-01 and GQDs-02 batches, as reported in Table 1. The larger GQDs-02, however, seem to give a slightly better agreement.

Employing b estimates from TEM measurements (Table 1, last column), we obtained reasonable values of the GQDs thickness a_i where the i index runs over the three possible models, in order. The Python script used to derive Table 1 results is available as SI.

Analysing the results, a discrepancy emerges between the simplified Stokes–Einstein equation using only the equivalent radius r_{eq} and the more refined models, such as the Perrin-Gierer and de la Torre corrections. Given the absence of a definitive method to measure the thickness of GQDs in solution, and considering that they are plausibly at least as thick as a single graphene layer, the Stokes–Einstein predictions appear unreliable. Furthermore, it remains uncertain whether the predominant fraction of nanoparticles in the GQDs samples consists of single or multilayer structures. Nonetheless, the findings consistently support the presence of a disk-like morphology, even in moderately alkaline environments.

4. Conclusions

In this study, we utilize the *D*-SPR approach for the first time as an effective method to characterize the size of GQDs and to provide indirect insights into their shape. Through meticulous microwave-assisted synthesis, two distinct batches of GQDs were produced and analyzed. The two batches chosen differ significantly in size, as independently verified by HR-TEM and DLS, enabling comparison across methods. Our results show excellent agreement between *D*-SPR and established techniques, supporting the validity of the method. HR-TEM analyses confirmed the general disk-like morphology of the nanoparticles, and advanced mathematical modeling applied to *D*-SPR data allowed precise measurements of their dimensions. This application of *D*-SPR complements traditional characterization methods such as DLS and HR-TEM, providing additional, quantitative information on particle size and distribution. The present work establishes proof-of-concept validating the *D*-SPR method to assess the size and size distribution of two representative batches of carbon-based nanomaterials with distinct structural features. Future studies will extend *D*-SPR to additional classes of nanoparticles. Furthermore, our results pave the way for *D*-SPR application in nanomaterials research, offering potential insights into structure–property relationships.

Conflicts of interest

There are no conflicts to declare.

Data availability

The XPS data supporting this article have been included in the supplementary information (SI). Supplementary information is available. See DOI: https://doi.org/10.1039/d5nr03481g.

A ready-to-use, GUI-based, Python script that reproduces the computations in Table 1 is available inside the following GitHub repository: https://github.com/G-S-Basile/D-SPR. The batches of HR-TEM pictures that were used to build the size distribution histograms in Fig. 2c and g are available at the following Renater repository: https://filesender.renater.fr/?s=download&token=9b9a00a6-32b2-43c4-a359-8b216ad16a6b.

Acknowledgements

The authors gratefully acknowledge funding from Société d'Accélération du Transfert de Technologies SATT Sayens (GREEN-CQDs project) and the University of Lorraine

(CAPTUR project) for the development of GQD-based materials. We also thank Aurélien Renard from the Spectroscopy and Microscopy Service Facility of SMI LCPME (Université de Lorraine–CNRS) for his valuable support. We also thank Grégory Francius from the Spectroscopy and Microscopy Service Facility (SMI) of LCPME for AFM measurements.. This research was supported by MIUR, PRIN: P2022AW2H9 "Molecular details on the early phase of amyloid beta peptides aggregation: a multilevel approach based on carbon dots fluorescence and diffusion coefficients measurements to unveil the pathogenic molecular mechanisms at the base of Alzheimer's disease" and "Progetto Pharma-HUB – HUB per il riposizionamento di farmaci nelle malattie rare del Sistema nervoso in età pediatrica" (T4-AN-04).

References

1 X. Xu, R. Ray, Y. Gu, H. J. Ploehn, L. Gearheart, K. Raker and W. A. Scrivens, *J. Am. Chem. Soc.*, 2004, **126**, 12736–12737.
2 S. Wang, I. S. Cole and Q. Li, *RSC Adv.*, 2016, **6**, 89867–89878.
3 P. Pierrat and J.-J. Gaumet, *Tetrahedron Lett.*, 2020, **61**, 152554.
4 P. Magri, P. Franchetti, J.-J. Gaumet, B. Maxit, S. Diliberto and P. Pierrat, *Appl. Sci.*, 2024, **14**, 8807.
5 G. S. Basile, D. Calcagno, I. Pandino, A. Pietropaolo, G. Schifino, N. Tuccitto, G. A. Zingale and G. Grasso, *Chemistry*, 2024, e202402346.
6 G. A. Zingale, I. Pandino, D. Calcagno, M. L. Perina, N. Tuccitto and G. Grasso, *PLoS One*, 2025, **20**, e0312594.
7 D. Calcagno, M. L. Perina, G. A. Zingale, I. Pandino, N. Tuccitto, V. Oliveri, M. C. Parravano and G. Grasso, *Protein Sci.*, 2024, **33**, e4962.
8 D. Calcagno, M. L. Perina, A. Distefano, M. Parravano, A. Licciardello, N. Tuccitto and G. Grasso, *Chem.:Methods*, 2025, **5**, e202400034.
9 G. S. Basile, D. Calcagno, N. Tuccitto, D. Sbardella and G. Grasso, *ChemPhysChem*, 2025, **26**, e202500138.
10 G. I. Taylor, *Proc. R. Soc. London, Ser. A*, 1953, **219**, 186–203.
11 G. A. Zingale, I. Pandino, A. Distefano, N. Tuccitto and G. Grasso, *Biosens. Bioelectron.:X*, 2023, **13**, 100306.
12 D. Calcagno, V. Oliveri, M. C. Parravano, N. Tuccitto and G. Grasso, *Biosens. Bioelectron.*, 2026, **292**, 118080.
13 M. S. Bello, R. Rezzonico and P. G. Righetti, *Science*, 1994, **266**, 773–776.
14 J. Stetefeld, S. A. McKenna and T. R. Patel, *Biophys. Rev.*, 2016, **8**, 409–427.
15 D. Geißler, C. Gollwitzer, A. Sikora, C. Minelli, M. Krumrey and U. Resch-Genger, *Anal. Methods*, 2015, **7**, 9785–9790.
16 K. Kurihara and K. Suzuki, *Anal. Chem.*, 2002, **74**, 696–701.
17 P. Singh, *Sens. Actuators, B*, 2016, **229**, 110–130.
18 G. A. Zingale, I. Pandino, D. Calcagno, M. L. Perina, N. Tuccitto and G. Grasso, *PlosOne*, 2025, **20**, e0312594.
19 M. Shamsipur, A. Barati and S. Karami, *Carbon*, 2017, **124**, 429–472.
20 Y. Sun, S. Wang, C. Li, P. Luo, L. Tao, Y. Wei and G. Shi, *Phys. Chem. Chem. Phys.*, 2013, **15**, 9907.
21 A. Liu, Z. Dai, D. Ouyang, B. Mahara, L. Yang and X. Chen, *Green Chem.*, 2025, **27**, 12460–12471.
22 J. G. Moberly, M. T. Bernards and K. V. Waynant, *J. Cheminf.*, 2018, **10**, 5.
23 A. Einstein, *Ann. Phys.*, 1905, **322**, 549–560.
24 M. Von Smoluchowski, *Ann. Phys.*, 1906, **326**, 756–780.
25 G. Chirico, M. Placidi and S. Cannistraro, *J. Phys. Chem. B*, 1999, **103**, 1746–1751.
26 A. Gierer and K. Wirtz, *Z. Naturforsch. A*, 1953, **8**, 532–538.
27 F. Perrin, *J. Phys. Radium*, 1936, **7**, 1–11.
28 A. Ortega and J. García De La Torre, *J. Chem. Phys.*, 2003, **119**, 9914–9919.
29 M. M. Tirado, C. L. Martínez and J. G. De La Torre, *J. Chem. Phys.*, 1984, **81**, 2047–2052.
30 M. M. Tirado and J. G. De La Torre, *J. Chem. Phys.*, 1979, **71**, 2581–2587.